Ray-tracing Based RIS Size, Placement and Target Point Optimization for Indoor Coverage Enhancement

EMRE KILCIOGLU, AND CLAUDE OESTGES

ICTEAM/ELEN, Université catholique de Louvain, Louvain-la-Neuve, Belgium

CORRESPONDING AUTHOR: E. KILCIOGLU (e-mail: emre.kilcioglu@uclouvain.be)

ABSTRACT Reconfigurable Intelligent Surfaces (RISs) have emerged as a transformative technology for enhancing wireless communication performance in complex indoor environments. However, the effectiveness of RIS deployment depends on several key factors, including the position, size, and target beam-steering points. Existing research often optimizes RIS phase profiles while assuming fixed positions and sizes, limiting the degrees of freedom for performance improvement. To address this gap, this paper proposes a novel ray-tracing based joint optimization framework that simultaneously determines the sub-optimal RIS position, size, and target points to enhance indoor coverage, particularly in blind spots. The proposed method integrates a clustering-based approach to identify low-power regions and determine optimal RIS beam-steering targets using the K-means algorithm. Feasible RIS positions that maintain line-of-sight (LoS) connections with both the transmitter and target points are selected, and the RIS size is iteratively adjusted to balance performance gains with hardware costs. Unlike population-based metaheuristic methods, which require extensive parameter tuning, the proposed approach leverages ray-tracing simulations to provide physically consistent and computationally efficient optimization. Extensive simulations in an indoor office environment demonstrate that the proposed framework significantly improves coverage and signal quality by systematically configuring RIS deployment parameters. These findings underscore the potential of ray-tracing based optimization in practical RIS-aided wireless communication scenarios.

INDEX TERMS Coverage enhancement, coverage map, optimization algorithms, ray-tracing simulation, reconfigurable intelligent surface (RIS)

I. INTRODUCTION

IN recent years, the rapid evolution of wireless communications has led to an increasing demand for reliable, high-capacity indoor connectivity. However, indoor environments present significant challenges due to complex geometries and numerous obstacles, such as walls, furniture, and other structural elements, which cause severe multipath fading and coverage blind spots [1]. These blind spots result in poor signal quality and reduced data rates, which are particularly problematic in densely populated or mission-critical indoor scenarios.

Reconfigurable intelligent surfaces (RISs) have emerged as a promising solution to address these challenges [2]. An RIS is typically a planar array of nearly passive, low-cost reflecting elements that can be programmed to manipulate the phase and amplitude of incident electromagnetic waves [3]. By dynamically adjusting these parameters, an RIS can create virtual line-of-sight (LoS) paths and steer reflected signals into areas with low received power, thereby improving overall coverage, signal-to-interference-noise ratio (SINR), spectral efficiency, and other performance metrics [4]. Unlike conventional active relays or phased array systems, which require power-hungry RF chains, RISs operate nearly passively by intelligently reflecting incident signals, thus reconfiguring the radio environment in a cost-effective and energy-efficient manner [5]. In indoor settings, this capability is especially

valuable, as it allows signals to be redirected into poor coverage areas, improving overall performance without the need for additional active components. Early work in this field has established the physical foundations of RISs, including their modeling and path-loss models [6]–[8], demonstrating that by engineering the reflection coefficients of a large number of subwavelength elements, RISs can create a "smart radio environment" where the wireless channel becomes programmable [9].

To achieve this programmable wireless environment, two principal electromagnetically consistent approaches have emerged for configuring RIS reflection coefficients via phase profile design, each offering distinct advantages for different deployment scenarios. The first approach, known as the phase-gradient-based method, treats the RIS as an ideal phase gradient reflector, introducing a controlled phase variation across the surface to achieve anomalous reflection [10]. By calculating phase shifts based on the relationship between incident and desired reflection directions, this method effectively steers reflected beams in desired directions, making it suitable for scenarios that require precise directional control. In contrast, the second method, the distance-based approach, configures the phase profile so that the electric fields of all paths from the RIS elements add up coherently to create constructive interference at a specific point in the scene, tuning the total distance traveled by each path to maximize power at that point [8]. While phase-gradient-based approach shines for the scenarios requiring specific reflection angles and broader coverage, the distance-based approach is particularly effective when precise focusing of reflected signals is needed, such as in indoor environments with specific blind spots.

In indoor scenarios, RIS design and placement are critical to maximizing their benefits. To optimize RIS placement, initial studies suggest that positioning the RIS near the access point (AP) or blind spots where the coverage enhancement is needed yields better communication performance due to the path loss law governing RIS-aided links [11], [12]. However, this may not be the optimal choice, considering the complexity of indoor environments, where a direct link is often hard to achieve.

A substantial amount of research has focused on various aspects of RIS optimization, including RIS phase profile (i.e., phase shift), RIS size or the number of RISs, and RIS position within the scene. The detailed literature review on RIS optimization can be found in Table 1, which covers a range of performance metrics such as transmit power [13], [14], [35], achievable rate [16], [17], [20], [27], signal-to-noise ratio (SNR) [18], [32]–[34], secrecy rate [19], [28], [29], sum-rate [21]–[26], [37], [38], energy efficiency [20], [30], number of RIS elements [21], [48], outage probability [31], [47], and coverage [37]–[46]. Several optimization techniques have been proposed for these problems, including deep reinforcement learning (DRL) [17], [18], [30], [36], alternating optimization (AO) [16], [22]–[24], [26], [32],

TABLE 1. Related works on RIS optimization

Paper	Phase Profile Opt.	Size or Number Opt.	Position Opt.
[13]–[19]	✓		
[20], [21]	✓	✓	
[22]–[44]	✓		✓
[45]–[49]	✓	✓	✓

sequential rotation algorithms [15], supervised learning [44], and graph theory [45], [46]. However, several issues with these studies remain, as summarized below:

- Many studies focus on optimizing transmit beamforming and the RIS phase profile, but fail to optimize the number of tunable elements in the RIS.
- Research that does not consider position optimization assumes the RIS is deployed at a fixed location, which constrains optimization to the phase domain and limits the degrees of freedom available for performance enhancement.
- Many papers use simplified channel models with certain assumptions, overlooking the realistic characterization of an environment and failing to account for both LoS and non-LoS (NLoS) paths. Most studies assume only LoS paths contribute, disregarding strong NLoS paths.

In addition to deterministic approaches, population-based metaheuristic methods, such as differential evolution (DE) algorithm [50], [51], genetic algorithm (GA) [52], [53], and particle swarm optimization (PSO) [54]–[56], have been applied to the RIS placement problem. These methods typically begin with a large, randomly generated population of candidate solutions, each representing a possible RIS position, and then iteratively refine these candidates through evolutionary operators or velocity updates. Although they are robust in navigating highly non-convex search spaces, they require many iterations and careful parameter tuning (e.g., mutation rates and crossover probabilities), and their convergence behavior is inherently stochastic. This means that their convergence can vary from run to run.

Although some studies jointly optimize RIS parameters, including phase profile, size, and position (as summarized in Table 1), tuning all these parameters together are needed, which leads to a highly non-convex optimization problem. Therefore, this optimization must be carried out in a realistic environment that considers all the propagation characteristics of the scene.

To address this challenge, incorporating RISs into ray-tracing based simulation tools is an essential step for realistic performance evaluation [57]. Ray-tracing models can accurately capture the propagation characteristics of indoor environments, enabling precise optimization of RIS properties and providing realistic performance measurements [58], [59]. Our previous work [60] introduced a ray-tracing based framework to enhance coverage in blind spots by selecting

optimal target points for RIS design. This framework involves a clustering-based algorithm that identifies low-power cells based on the transmitter-only coverage map and groups them by coordinates to define potential RIS beam steering target points using the K-means algorithm. A ray-tracing based search algorithm then determines a sub-optimal RIS size based on fixed transmitter and RIS positions. However, that study assumed a fixed RIS position, which limited the optimization process's flexibility.

In this extended study, we propose a novel ray-tracing based joint optimization framework that simultaneously determines the sub-optimal RIS position, size, and number of target points to maximize average coverage in the least covered areas (i.e., blind spots). First, after obtaining the transmitter-only coverage map, the clustering-based algorithm from our previous work [60] is used to identify and group low-power cells into RIS target points. Then, feasible RIS positions that maintain LoS connections with both the transmitter and all target points are searched. Additionally, we iteratively adjust the RIS size to balance performance gains with hardware costs, selecting a sub-optimal RIS size based on a predefined performance improvement threshold. Unlike prior works that assume a fixed RIS position or arbitrary RIS sizes, our approach systematically determines all key RIS parameters in a unified framework by using a ray-tracing based realistic environment, considering both LoS and NLoS paths.

Compared to population-based metaheuristic methods like DE, GA or PSO, our algorithm reduces the search space by first identifying low-power regions where signal enhancement is most needed. It then constrains the set of feasible RIS positions by enforcing a LoS condition to both the transmitter and all target points, further narrowing the search space. This structure-aware approach leads to faster convergence than generic metaheuristic methods. Evaluation in our algorithm is carried out through ray-tracing simulations to compute a performance metric, the average power of low-power cells, ensuring that only physically feasible and high-performing configurations are selected.

The main contributions of this paper can be summarized as follows:

- We introduce a ray-tracing based RIS optimization algorithm that jointly optimizes the RIS position, size, and target points to enhance blind spot coverage in indoor environments.
- The proposed method incorporates a clustering-based approach to identify low-power regions and determine optimal RIS beam steering target points using the K-means algorithm.
- We present a performance-cost trade-off strategy that selects a sub-optimal RIS size, considering a performance improvement threshold to avoid diminishing returns from further size increases.
- Extensive simulations in an indoor office scenario demonstrate the effectiveness of the proposed algo-

rithm, showing significant coverage improvements by placing the RIS in a sub-optimal location with an appropriate size and configuring it to steer beams towards selected target points, potentially covering all blind spots within the scene.

The remainder of this paper is organized as follows: Section II explains the integration of the RIS into the ray-tracing tool. Section III provides a detailed mathematical modeling of two RIS phase profile configuration methods for steering beams towards desired target points. Section IV describes the proposed joint optimization framework, including the underlying ray-tracing methodology and the optimization algorithm. Extensive simulation results are presented in Section V. Finally, Section VI concludes the paper and outlines future research directions.

II. RIS INTEGRATION INTO THE RAY-TRACING TOOL

This section outlines the integration of an RIS into the ray-tracing simulation tool. We choose to work with NVIDIA's open-source Sionna ray-tracing tool [61] due to its user-friendly structure and the ability to change internal parameters of the tool according to our use.

In an indoor environment, transmitter-only coverage maps reveal blind spots which are the areas with inadequate signal quality caused by obstacles such as walls or large furniture that block line-of-sight (LoS) paths between the transmitter and these regions. To address this, an RIS can be strategically positioned to create virtual LoS paths, reflecting signals from the transmitter to these blind spots. By configuring the RIS to direct reflected signals into these areas, the average signal power in blind spots and the overall coverage ratio can be improved through the combined contributions of the transmitter and RIS. In this paper, the considered performance metric is the average power of these blind spots, and the aim is to maximize this metric by optimizing the position, size, and target point selection of the RIS.

To incorporate the RIS into the ray-tracing tool, the surface is discretized into a grid of $N \times M$ tiles, each with dimensions d_y and d_z, as shown in Fig. 1. Each tile, denoted as $T_{n,m}$ for the nth row and mth column, is characterized by a complex reflection coefficient that controls the amplitude and phase of incoming electromagnetic waves to reflect the signal to the desired target points. The discretization approach approximates a continuous surface when d_y and d_z are sufficiently small, which provides precise control over the reflected wavefronts. Without loss of generality, in this paper, the RIS is assumed to be placed in the y-z plane of the 3D simulation scenario.

The RIS's reflection behavior is determined by the collective contribution of its tiles, which are configured to reflect signals toward $K \geq 1$ target points. For simplicity, Fig. 1 illustrates a single target point, although we consider multiple target points in this paper to address multiple blind spots. The complex reflection coefficient for a single tile,
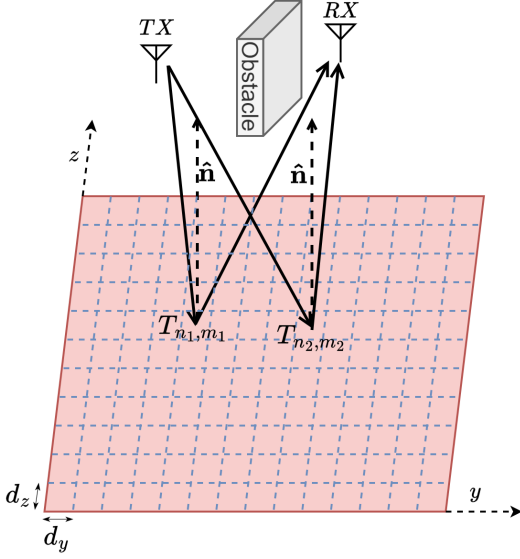
FIGURE 1. Illustration of RIS modeling: The RIS surface is discretized into tiles, each with tunable reflection characteristics, to direct signals toward the target points.

$\Gamma_{n,m}$, is expressed as

$$\Gamma_{n,m} = \sum_{k=1}^{K} \sqrt{c_k} A_{n,m}^k e^{j\varphi_{n,m}^k} \qquad (1)$$

where $A_{n,m}^k$ and $\varphi_{n,m}^k$ represent the amplitude and phase assigned for the kth target point, respectively. These assignments collectively form the 2D amplitude profile $\mathbf{A}^k$ and the phase profile $\mathbf{\Phi}^k$ for the RIS to reflect the signal into the kth target point. The power intensity coefficient c_k, which determines the power allocated to each target point, satisfies the following:

$$\sum_{k=1}^{K} c_k = 1 \qquad (2)$$

The overall reflection coefficient $\mathbf{\Gamma}$ of the RIS is computed as the weighted sum of the individual amplitude and phase profiles for all target points, with weights given by the power intensity coefficients c_k.

The considered RIS modeling enables the simulation of various RIS configurations in different environments. For instance, in complex indoor scenarios with significant obstructions, the RIS can mitigate blind spots by steering reflected signals around obstacles into otherwise unreachable areas. Through careful design of amplitude and phase profiles, the RIS enhances received signal power in these areas and addresses shadowing effects.

III. RIS PHASE PROFILE CONFIGURATION METHODS

In RIS modeling, the primary focus is on the phase change introduced to the incoming signal, as the amplitude is typically assumed to remain constant, generally between 0.8 and 1. Therefore, the design and optimization of RIS are centered on assigning appropriate phase profiles to control the direction and behavior of reflected waves.

In this section, we consider two primary methods for configuring the phase profiles $\mathbf{\Phi}^k$ of the RIS to achieve anomalous reflections for each target point k: the gradient-based phase profile [10] and the distance-based phase profile [8]. These methods offer distinct advantages, making them suitable for different environmental scenarios and system requirements.

1) **Gradient-based Phase Profile**: This method considers the incidence and desired reflection wave directions, and it aims to achieve the desired reflection direction by introducing a phase gradient across the RIS. The phase gradient is computed to align the reflected signal with the desired reflection direction, thereby optimizing the coverage at the target points.

2) **Distance-based Phase Profile**: In contrast to the gradient-based method, the distance-based method focuses on the total distance traveled by the incident and reflected signals. By adjusting the phase shifts to match the distances from the transmitter to each tile and from each tile to a specific target point, the method ensures that the reflected signals constructively interfere at this target point location.

The phase profile for these methods is computed for each target point k, and the individual phase profiles are combined through the summation in (1) to derive the overall reflection coefficient profile $\mathbf{\Gamma}$.

A. GRADIENT-BASED PHASE PROFILE

The gradient-based method, as illustrated in Fig. 2, treats the RIS as an ideal phase gradient reflector. The phase gradient is calculated based on the incident wave direction and the desired reflection direction for each target point. In this method, the RIS introduces a phase gradient that modifies the direction of the reflected waves, aiming to direct the reflected signal toward a desired target point.

Let us consider an incident wave with wave vector $\hat{\mathbf{k}}_i$ arriving at the center of the RIS at an incidence angle θ_i with respect to the RIS normal vector $\hat{\mathbf{n}}$. The desired reflection direction for the target point k is represented by the reflection wave vector $\hat{\mathbf{k}}_r$ with a reflection angle θ_r. The incident phase gradient due to the inclined wavefront is given by

$$\nabla\varphi_i = -k_0 \sin\theta_i \, \hat{\mathbf{k}}_i^p = -k_0 \, \mathbf{P}\hat{\mathbf{k}}_i \qquad (3)$$

where $k_0 = 2\pi/\lambda$ is the wavenumber and λ is the wavelength. Here, $\hat{\mathbf{k}}_i^p$ represents the unit projection of the incident wave vector $\hat{\mathbf{k}}_i$ onto the plane of the RIS, and $\mathbf{P}$ is the projection operator, where $\mathbf{P}\hat{\mathbf{k}}_i = \sin\theta_i \, \hat{\mathbf{k}}_i^p$.

The RIS applies an additional phase gradient $\nabla\varphi_{RIS}$, which adjusts the reflection direction to achieve the desired angle θ_r. Then, the reflection phase gradient $\nabla\varphi_r$ becomes

$$\nabla\varphi_r = \nabla\varphi_i + \nabla\varphi_{RIS} \qquad (4)$$
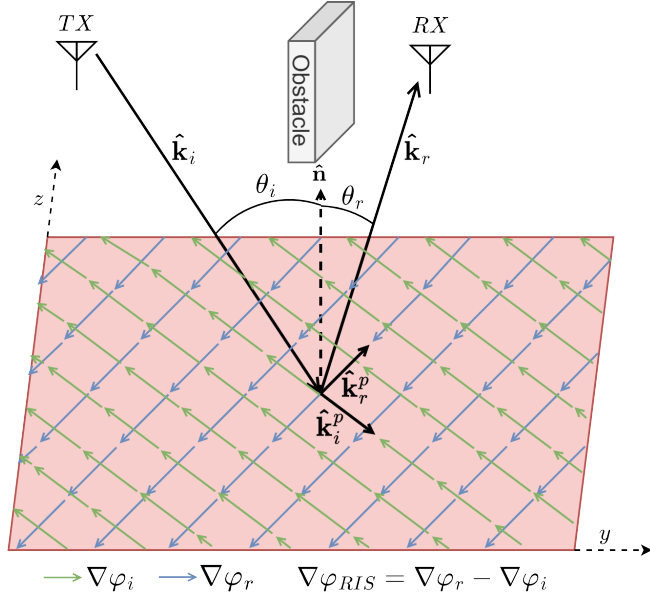
FIGURE 2. The gradient-based method for configuring the RIS phase profile to reflect signals toward the target point

Similar to (3), the reflection phase gradient $\nabla \varphi_r$ is expressed as

$$\nabla \varphi_r = -k_0 \ \sin \theta_r \ \hat{\mathbf{k}}_r^p = -k_0 \ \mathbf{P}\hat{\mathbf{k}}_r \tag{5}$$

where $\hat{\mathbf{k}}_r^p$ is the unit projection vector of the reflection wave vector $\hat{\mathbf{k}}_r$ onto the RIS. By substituting (3) and (5) into (4), we find the desired phase gradient onto the RIS to reflect the incoming wave with direction $\hat{\mathbf{k}}_i$ to the reflection wave with direction $\hat{\mathbf{k}}_r$

$$\nabla \varphi_{RIS} = k_0 \ \mathbf{P}(\hat{\mathbf{k}}_i - \hat{\mathbf{k}}_r) = k_0 \ (\sin \theta_i \ \hat{\mathbf{k}}_i^p - \sin \theta_r \ \hat{\mathbf{k}}_r^p) \tag{6}$$

For simpler cases, such as when the RIS, transmitter, and target positions are assumed to be at the same height, the phase gradient onto the RIS becomes one-dimensional along the y-axis, which can be shown as follows:

$$\nabla \varphi_{RIS} = k_0 \left(\sin \theta_i - \sin \theta_r\right) \hat{y} \tag{7}$$

This simplification results in a one-dimensional phase gradient and a more straightforward implementation of the RIS design.

The phase profile $\mathbf{\Phi}^k$ for each target point k is then generated by setting the first RIS tile phase to zero and applying a linear variation of the phase across the surface, following the gradient calculated in (6) or (7).

B. DISTANCE-BASED PHASE PROFILE

The distance-based method models the RIS as a focusing lens that ensures the reflected signals combine constructively at the target point. By calculating the phase shift required at each tile, this method ensures that the signals from all tiles travel the same total distance, ensuring constructive interference at the target point.

The position of each tile $T_{n,m}$ relative to the RIS center is given by $(0, (m-\frac{1}{2})d_y, (n-\frac{1}{2})d_z)$, where $m \in \left[1 - \frac{M}{2}, \frac{M}{2}\right]$

and $n \in \left[1 - \frac{N}{2}, \frac{N}{2}\right]$ represent the row and column indices of the tile, assuming that the center of the coordinate system is taken as the center of the RIS without loss of generality.

The electric field arriving at each tile $T_{n,m}$ is expressed as

$$E_{n,m}^{in} = \sqrt{\frac{2Z_0 P_{n,m}^{\text{TX-RIS}}}{d_y d_z}} e^{-j \frac{2\pi r_{n,m}^{tx}}{\lambda}} \tag{8}$$

where Z_0 is the characteristic impedance of free space, $r_{n,m}^{tx}$ is the distance between the transmitter and $T_{n,m}$, and $P_{n,m}^{\text{TX-RIS}}$ is the received power of the incident wave at each tile. After reflection, the total electric field at the desired target point is

$$E^{rx} = \sum_{n=1-\frac{N}{2}}^{\frac{N}{2}} \sum_{m=1-\frac{M}{2}}^{\frac{M}{2}} E_{n,m}^{rx} \tag{9}$$

where each reflected field, contributed by $T_{n,m}$ is:

$$E_{n,m}^{rx} = \sqrt{\frac{2Z_0 P_{n,m}^{rx}}{A_{rx}}} e^{-j\left(\frac{2\pi}{\lambda}(r_{n,m}^{tx}+r_{n,m}^{rx})-\varphi_{n,m}^{k}\right)} \tag{10}$$

where $r_{n,m}^{rx}$ is the distance from $T_{n,m}$ to the receiver, A_{rx} is the receiving antenna aperture, and $P_{n,m}^{rx}$ is the power of the reflected signal of $T_{n,m}$ at the desired target point and can be expressed as

$$P_{n,m}^{rx} = P_{n,m}^{\text{RIS-RX}}(A_{n,m}^{k})^2 P_{n,m}^{\text{TX-RIS}} \tag{11}$$

where $P_{n,m}^{\text{RIS-RX}}$ is the multiplicative factor to the received power of the path from $T_{n,m}$ to the desired target point. The combined received power of all tiles at target point k is then given by

$$P^{rx} = \frac{|E^{rx}|^2}{2Z_0} A_{rx}$$

$$= \left| \sum_{n=1-\frac{N}{2}}^{\frac{N}{2}} \sum_{m=1-\frac{M}{2}}^{\frac{M}{2}} A_{n,m}^{k} \sqrt{P_{n,m}^{\text{TX-RIS}} P_{n,m}^{\text{RIS-RX}}} \right. \tag{12}$$

$$\left. \times e^{-j\left(\frac{2\pi}{\lambda}(r_{n,m}^{tx}+r_{n,m}^{rx})-\varphi_{n,m}^{k}\right)} \right|^2$$

In the distance-based phase profile method, the aim is to maximize the combined received power P^{rx} in (12), which is maximized when the imaginary part of each term in the summation is tuned in. Then, the following phase assignment for each tile holds:

$$\varphi_{n,m}^{k} = \frac{2\pi}{\lambda}(r_{n,m}^{tx} + r_{n,m}^{rx}) \tag{13}$$

where the phase profile $\mathbf{\Phi}^k$ is created by assigning this expression to each tile to achieve constructive interference at the desired target point.

IV. JOINT RIS SIZE, POSITION AND TARGET POINT OPTIMIZATION ALGORITHM

In a typical indoor scenario, the transmitter's position is assumed to be fixed in this paper. Then, we can easily simulate the transmitter-only coverage map in the ray-tracing tool and reveal the scenario's blind spots with insufficient signal

power that require coverage enhancement. The objective of this study is to utilize RIS deployment to improve the signal power in these blind spots, ensuring acceptable signal quality throughout all the areas in the scene.

In our previous work [60], we addressed this issue by introducing a method to identify blind spots based on the transmitter-only coverage map. By defining a minimum power threshold for acceptable signal quality, regions with power levels below this threshold were classified as low-power cells which require coverage enhancement. The coordinates of these low-power cells were then grouped into a fixed number of clusters using the K-means clsutering algorithm, and the centroids of these clusters were selected as the target points for the RIS. However, the position of the RIS in [60] was assumed to be fixed, which limited the flexibility of the solution.

To overcome this limitation, we propose a novel algorithm in this study that jointly optimizes the RIS size, position, and number of target points. The algorithm first identifies low-power cells based on the transmitter-only coverage map. For each possible number of target points, it searches for feasible RIS positions within the scene that maintain a line-of-sight (LoS) connection with both the transmitter and all target points. Each feasible configuration of RIS position and number of target points is evaluated for each searched RIS size. The best configuration defined by the RIS position and number of target points is selected for each RIS size. Subsequently, the RIS size is varied iteratively, and the performance improvement is assessed. When the performance improvement falls below the defined threshold, the corresponding RIS size is selected as the sub-optimal size. This approach not only seeks to improve coverage but also balances performance gains with hardware cost by determining a sub-optimal RIS size. Increasing the RIS size enhances coverage, but after a certain point, the performance improvement becomes marginal compared to the added cost. Hence, the proposed algorithm identifies the trade-off point between performance and cost by defining a performance improvement threshold. This threshold manages the decision to continue increasing the RIS size. Without loss of generality, this study varies the RIS size by adjusting its width while keeping its height fixed, allowing for a clear analysis of one-dimensional size variations. However, the approach can be extended to two-dimensional size adjustments, where both height and width are increased proportionally. Detailed steps of the proposed algorithm are presented in Algorithm 1-2.

V. SIMULATION RESULTS

A. SIMULATION SCENARIO

In this paper, we consider a U-shaped indoor office scenario consisting of three main hallways: the 'upper' and 'lower' hallways, which form the two arms of the U, and the 'intersecting' hallway that connects them at the bottom. Additionally, there is an internal room located at the intersection

---

Algorithm 1: Ray-tracing Based RIS Size, Position and Target Points Optimization (Part 1)

Input:
- **The scene geometry:** A 3D representation of the area where coverage is to be enhanced, including obstacles, walls, etc.
- **Transmitter (TX) position:** Coordinates of the transmitter in the scene.
- **Minimum power threshold P_{th}:** The threshold for acceptable signal power, below which cells are considered low-power.
- **Range of possible target points $\mathcal{N}$:** The set of possible cluster counts to be used in K-means algorithm, e.g., $\mathcal{N} = \{1, 2, \ldots, 5\}$.
- **Set of possible RIS widths $\mathcal{W}$:** The set of candidate RIS widths, e.g., $\mathcal{W} = \{0.2, 0.4, \ldots, 3.0\}$ m.
- **Minimum performance improvement threshold $\Delta\mathcal{M}_{\text{min}}$:** The minimum performance improvement required to justify increasing the RIS width.

Output:
- **Sub-optimal number of target points N^{opt}.**
- **Sub-optimal RIS width $W_{\text{RIS}}^{\text{opt}}$.**
- **Sub-optimal RIS position $\mathbf{r}_{\text{RIS}}^{\text{opt}}$.**

Compute the transmitter-only coverage map $\mathbf{P}_{\text{TX}}(x, y)$.

Set a minimum power threshold P_{th} for acceptable signal quality.

Identify low-power cells in $\mathbf{P}_{\text{TX}}(x, y)$ where the power level is below the minimum power threshold P_{th}, denoted as $\mathcal{C}_{\text{low}}$:

$$\mathcal{C}_{\text{low}} = \{(x, y) \mid \mathbf{P}_{\text{TX}}(x, y) < P_{\text{th}}\} \qquad (14)$$

---

of these hallways. The layout of the scenario is illustrated in Fig. 3, where the transmitter position is marked with a blue circle, and an example RIS placement is represented by a purple rectangle on the intersecting hallway wall.

For the simulation environment, the materials used for the walls, floors, and ceilings are selected from a predefined list in Sionna RT, based on their typical usage in indoor environments and their electromagnetic properties. Sionna RT incorporates material models defined in the ITU-R P.2040-2 recommendation [62]. Specifically, the selected materials are:

- **Walls:** Plasterboard (*itu_plasterboard*) is chosen due to its common application in building interiors.
- **Floors:** Chipboard (*itu_chipboard*) is selected for its suitability and practicality as an indoor flooring material.
- **Ceilings:** Ceiling board (*itu_ceiling_board*) is used for its specific design for ceilings.

Algorithm 2: Ray-tracing Based RIS Size, Position and Target Points Optimization (Part 2)

---

foreach *number of target points* $N \in \mathcal{N}$ **do**
    Apply K-means algorithm to $\mathcal{C}_{\text{low}}$ to group the low-power cells into N clusters and obtain N centroids:

$$\text{K-means}(N, \mathcal{C}_{\text{low}}) \rightarrow \text{Centroids}\{\mathbf{c}_1, \mathbf{c}_2, \ldots, \mathbf{c}_N\} \quad (15)$$

    where each centroid $\mathbf{c}_i$ represents a target point where coverage enhancement is needed.
    Identify the set of feasible RIS positions $\mathcal{R}_N$ that provide line-of-sight (LoS) to both the transmitter and all N target points:

$$\mathcal{R}_N = \{\mathbf{r}_{\text{RIS}} \mid \text{LoS}(\mathbf{r}_{\text{RIS}}, \mathbf{TX}) \wedge \text{LoS}(\mathbf{r}_{\text{RIS}}, \mathbf{c}_i) \, \forall \mathbf{c}_i\} \quad (16)$$

    foreach *RIS width* $W_{RIS} \in \mathcal{W}$ **do**
        Compute the combined coverage $\mathbf{P}_{\text{comb}}(x, y)$ at each low-power cell, considering both TX and RIS contributions, for each RIS position $\mathbf{r}_{\text{RIS}} \in \mathcal{R}_N$.
        Calculate the performance metric $\mathcal{M}(\mathbf{r}_{\text{RIS}}, N, W_{\text{RIS}})$ for all parameter combinations as the average power of low-power cells after placing the RIS at $\mathbf{r}_{\text{RIS}}$:

$$\mathcal{M}(\mathbf{r}_{\text{RIS}}, N, W_{\text{RIS}}) = \frac{1}{|\mathcal{C}_{\text{low}}|} \sum_{(x,y) \in \mathcal{C}_{\text{low}}} \mathbf{P}_{\text{comb}}(x, y) \quad (17)$$

    end
end
Identify the RIS configuration $(\mathbf{r}_{\text{RIS}}^{W_{\text{RIS}}}, N^{W_{\text{RIS}}}, W_{\text{RIS}})$ that maximizes the performance metric $\mathcal{M}$ for each W_{RIS}:

$$(\mathbf{r}_{\text{RIS}}^{W_{\text{RIS}}}, N^{W_{\text{RIS}}}) = \arg \max_{\mathbf{r}_{\text{RIS}} \in \mathcal{R}_N, N \in \mathcal{N}} \mathcal{M}(\mathbf{r}_{\text{RIS}}, N, W_{\text{RIS}}) \quad (18)$$

Select the smallest RIS width $W_{\text{RIS}}^{\text{opt}}$ for which increasing the RIS width further does not yield a performance improvement exceeding $\Delta \mathcal{M}_{\text{min}}$.
Assign corresponding parameters $\mathbf{r}_{\text{RIS}}^{\text{opt}} = \mathbf{r}_{\text{RIS}}^{W_{\text{RIS}}^{\text{opt}}}$ and $N^{\text{opt}} = N^{W_{\text{RIS}}^{\text{opt}}}$.

In this scenario, the transmitter is assumed to be placed at the intersection of the hallways on the upper side, as indicated by the blue circle in Fig. 3. This placement may result in potential blind spots with weak signal quality at the far edge of the lower hallway and certain areas within the internal room. To mitigate these blind spots, an RIS can be strategically positioned on the wall of the intersecting hallway, depending on the selected minimum power threshold value.
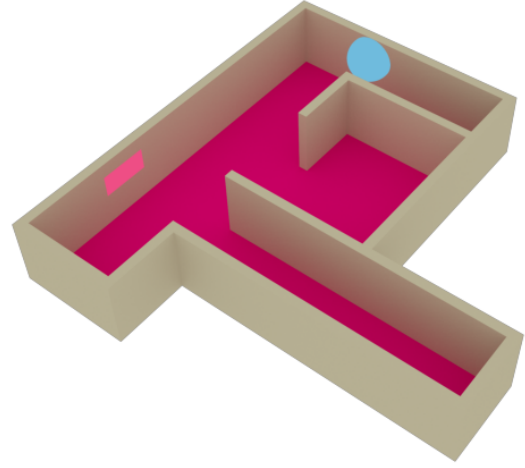

FIGURE 3. Scenario Illustration

B. GRAPHICAL USER INTERFACE (GUI) FOR SIMULATION RESULTS EXTRACTION

A Python-based graphical user interface (GUI) has been developed to facilitate the extraction and visualization of simulation results for the proposed algorithm. The main interface of this GUI is shown in Fig. 4. This interface allows users to load predefined scenarios, define the operating frequency of the scene, set the position of the transmitter, specify the minimum power threshold, and configure numerous other parameters.

After the necessary parameters are entered, the GUI provides several functionalities, including:

- Generating coverage map plots.
- Identifying the RIS target points using the K-means clustering algorithm, based on the distribution of low-power cells in the transmitter-only coverage map.
- Displaying feasible RIS positions depending on the location of the target points.

Furthermore, the GUI allows users to define the boundaries for optimization parameters related to the proposed algorithm in Section IV. These parameters include the number of target points, RIS width, and RIS position. The GUI computes performance metrics for all possible combinations of these parameters, enabling users to end up with suboptimal optimization configurations. Additionally, the GUI can visualize the effect of RIS width on performance metrics, as well as generate cumulative distribution functions (CDFs) for different phase profile approaches and RIS sizes.

The GUI is shared as an open-source project on GitHub and can be accessed at the following link: https://github.com/ekilcioglu/RIS-Optimization-GUI

C. SIMULATION PARAMETERS

The simulation parameters are carefully chosen to evaluate the performance of the proposed algorithm under realistic conditions. The amplitude profile of the reflection coefficients for each target point is set to unity to isolate and
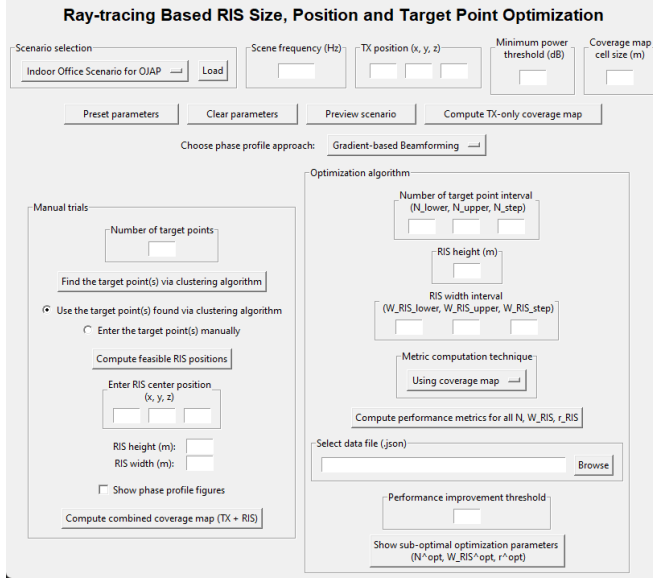
FIGURE 4. Illustration of the GUI interface

FIGURE 5. Transmitter-only coverage map

analyze the pure effect of the phase profiles. The power intensity coefficients, c_k, which determine how power is distributed among the target points, are set to equal values, ensuring identical importance is assigned to each blind spot in the scenario.

The system operates at a communication frequency of 5.8 GHz, corresponding to a wavelength of $\lambda = c/f = 5.17$ cm, where c is the speed of light. The RIS grid sizes, d_y and d_z, are defined as $\lambda/2 = 2.585$ cm.

Two distinct minimum power threshold values P_{th} are considered in the simulations:

- -100 dB: This threshold results in a higher number of low-power cells in the scene, providing a broader area for the RIS to enhance.
- -110 dB: This lower threshold value allows the RIS to focus on cells with comparably weaker power levels.

The results corresponding to these threshold values are simulated separately to assess the impact of power thresholds on the optimization and coverage enhancement provided by the RIS.

D. TRANSMITTER-ONLY COVERAGE MAP
The transmitter-only coverage map, which represents the power distribution from the transmitter without the assistance of an RIS, is depicted in Fig. 5. The transmitter position is marked with a red '+' sign. As observed in the figure, signal power decreases significantly in certain areas of the scenario, resulting in potential blind spots with weak signal coverage.

Specifically, these blind spots are primarily located at the far edge of the lower hallway and in several regions within the internal room. The presence of these blind spots highlights the limitations of transmitter-only coverage in complex indoor environments with non-line-of-sight (NLOS)
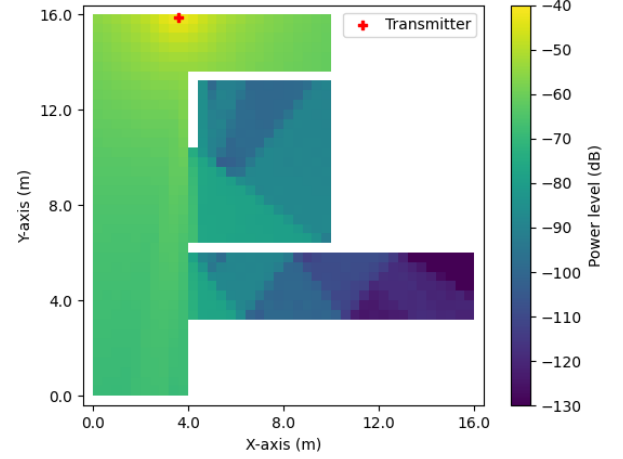
regions and significant signal attenuation caused by obstacles and walls. Such weak coverage can negatively impact the reliability and quality of communication in these areas.

To address these limitations, the strategic placement of an RIS becomes essential. By redirecting and enhancing the signal, the RIS can extend the coverage to include these blind spots, thereby improving the overall system performance. The selection of an optimal RIS placement depends on factors such as the spatial distribution of the low-power cells in the blind spots and the minimum power threshold values used in the simulations.

Fig. 5 serves as the baseline coverage map, against which the improvements brought by the RIS placement and optimization will be evaluated in subsequent sections.

E. RESULTS FOR MINIMUM POWER THRESHOLD OF -100 dB
1) BINARY POOR COVERAGE MAPS FOR DIFFERENT NUMBER OF TARGETS
For the simulations, we begin by assigning a minimum power threshold of -100 dB. As explained earlier, cells in the coverage map that fall below this threshold are categorized as low-power cells, which require a power boost for reliable communication. The distribution of these low-power cells is depicted in Fig. 6 for different numbers of target points N. These plots, referred to as binary poor coverage maps, visually represent the areas where the signal strength is below the threshold (red areas) and areas where the signal strength is acceptable (blue areas).

The positions of the low-power cells are clustered using the K-means algorithm, and the centroids of these clusters are marked as green 'x' symbols in Fig. 6. These centroids represent the target points where the RIS will steer its beams to improve signal coverage. Feasible RIS positions are then determined based on line-of-sight (LoS) visibility to both the target points and the transmitter. These positions are indicated by green star symbols on the same figure.
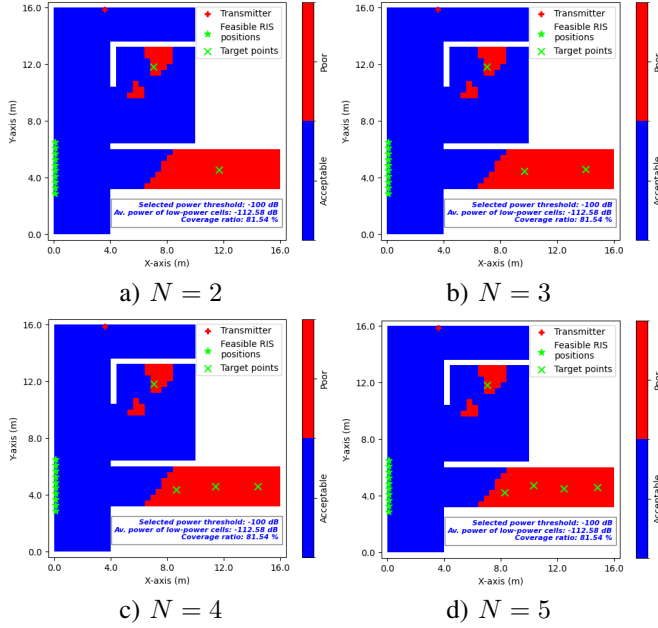
FIGURE 6. Binary poor coverage maps for different number of target configurations for the minimum power threshold of -100 **dB**

For each configuration shown in Fig. 6, the average power of the low-power cells is calculated as -112.58 dB, significantly below the set minimum power threshold of -100 dB.

In addition to the average power of the low-power cells, we also analyze a new metric known as the coverage ratio. The coverage ratio represents the percentage of the scene that is covered by either the transmitter or the RIS. The coverage ratio in the transmitter-only coverage map for the consideration of the minimum power threshold of -100 dB is 81.54%, as seen in Fig. 6. This coverage ratio metric is crucial, as focusing only on the average power of low-power cells might lead to misleading results. For example, a higher average power could indicate an improvement in performance, but if many areas remain uncovered, the coverage ratio could still be limited. A situation like this might arise if the RIS concentrates on boosting the power of certain low-power cells, thus increasing their signal strength significantly, while leaving other low-power cells uncovered. Monitoring the coverage ratio reveals such scenarios and helps ensure that the optimization does not overlook areas that still lack coverage.

Although this issue can occur, it is generally rare because the RIS initially boosts the power level of any low-power cell it illuminates. However, after a certain point, focusing further on the same cell does not result in exponential power increases, as the RIS effect becomes saturated.

2) RIS OPTIMIZATION ALGORITHM RESULTS
After generating the transmitter-only coverage map, identifying the low-power cells, determining the target points, and

feasible RIS positions, the optimization algorithm proposed in Section IV is applied to calculate the performance metric $\mathcal{M}$. This metric is evaluated for all parameter combinations, including the number of target points, feasible RIS positions, and RIS width. For each RIS width, the configuration that maximizes $\mathcal{M}$ is identified as the sub-optimal configuration for that specific width.

The results of the performance metric $\mathcal{M}$ for varying RIS widths are shown in Fig. 7, considering different RIS heights and phase profile approaches. It can be observed that the curves tend to saturate beyond a certain RIS width. Initially, increasing the RIS width significantly enhances the coverage by boosting the power level of low-power cells illuminated by the RIS. However, once most of these cells reach an acceptable power level, additional increases in RIS width do not contribute significantly to further improvements. This highlights the importance of considering the cost-effectiveness of increasing RIS width.

Another notable observation is that the gradient-based approach consistently outperforms the distance-based approach for the considered minimum power threshold of -100 dB. This is because the gradient-based approach not only boosts the power at the target points but also increases the power at other locations along the beam paths, covering a broader area. In contrast, the distance-based approach aims to create constructive interference specifically at the target points, which results in a more localized effect. While this approach leads to a significant power boost at the selected points, it does not effectively extend coverage to surrounding low-power cells, leaving some areas insufficiently illuminated. Despite this limitation, the distance-based approach still yields a noticeable improvement in performance. This difference between these phase profile approaches is particularly pronounced in scenarios where the low-power regions are large, making the gradient-based approach more effective in such cases.

The impact of RIS height is also more noticeable in the distance-based approach compared to the gradient-based approach. Specifically, when the RIS height is increased from 0.5 m to 1 m, the improvement in performance is more significant for the distance-based approach. In contrast, for the gradient-based approach, a smaller RIS height provides nearly equivalent performance, suggesting that a lower RIS height can be selected in such cases to balance performance with practical deployment constraints.

Next, in Fig. 8, the gradient-based approach for an RIS height of 1 m is analyzed in detail. The figure highlights the configurations that maximize the performance metric $\mathcal{M}$ for each RIS width. The annotations in the figure indicate the optimal RIS positions (denoted as "RIS pos") and the number of target points for different widths as well as the corresponding coverage ratio.

To determine the sub-optimal RIS width, a performance improvement threshold $\Delta\mathcal{M}_{\min}$ is introduced. This threshold represents the minimum performance gain required to
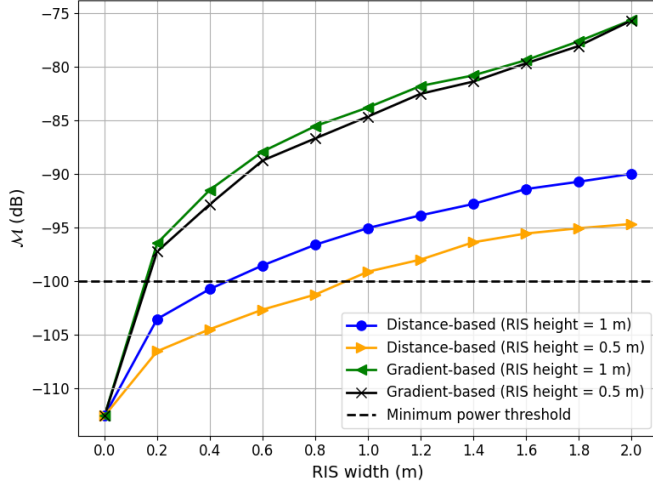
FIGURE 7. Performance metric $\mathcal{M}$ as a function of RIS width for different RIS heights and phase profile approaches, with a minimum power threshold of -100 dB
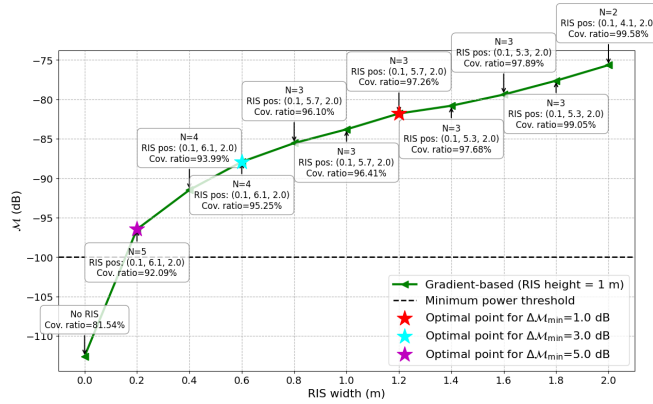

FIGURE 8. Performance metric $\mathcal{M}$ vs. RIS width for the gradient-based approach, showing selected sub-optimal configurations for different performance improvement thresholds $\triangle\mathcal{M}_{\mathbf{min}}$ with an RIS height of 1 m and a minimum power threshold of -100 dB

FIGURE 9. Performance metric $\mathcal{M}$ vs. RIS width for the distance-based approach, showing selected sub-optimal configurations for different performance improvement thresholds $\triangle\mathcal{M}_{\mathbf{min}}$ with an RIS height of 1 m and a minimum power threshold of -100 dB

justify increasing the RIS width to the next level. Higher thresholds lead to smaller RIS widths with slightly reduced performance, as increasing the RIS width further does not provide sufficient improvement to justify the additional cost. As seen in Fig. 8, even a minimal RIS width of 0.2 m significantly boosts $\mathcal{M}$ compared to the transmitter-only case (No RIS). Furthermore, the coverage ratio improves significantly, reaching nearly 100% at larger RIS widths, demonstrating the effectiveness of the optimization algorithm.

Also, the number of target points are assigned less and less with increasing the RIS width. This is because initially, the RIS width is not enough to cover the large area of blind spots, that's why the RIS is assigned to more number of target points to cover all of the region. However, after increasing the RIS width, since the thickness of the beam from the RIS increases, it becomes sufficient to obtain better performance results with a less number of targets without dividing the power allocated to each target point.
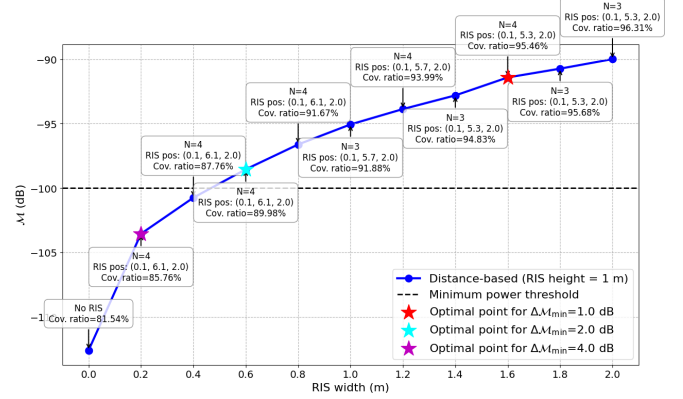
In Fig. 9, the distance-based approach is analyzed for an RIS height of 1 m. Similar trends are observed, with slightly lower performance metric values and coverage ratios compared to the gradient-based approach. This difference reflects the distance-based approach's narrower focus on the target points, which leaves some low-power cells uncovered.

3) CUMULATIVE DISTRIBUTION FUNCTION (CDF) ANALYSIS OF POWER LEVELS IN THE SCENE

To evaluate the impact of RIS placement on overall power distribution, we analyze the cumulative distribution function (CDF) of the power levels across the entire scene for different phase profile approaches and RIS sizes, as shown in Fig. 10. The RIS is positioned at its sub-optimal location for each size, as identified in Figs. 8 and 9. In the figure labels, the RIS size is denoted in the format 'height × width'.

The results indicate that the lowest power levels in the scene are significantly improved by both the distance-based and gradient-based approaches compared to the baseline case without RIS. This is because the RIS primarily targets low-power cells in blind spots, where signal coverage is weakest. The key difference between the two approaches is observed in the moderate power level range. While the gradient-based approach enhances power levels in these cells considerably, the distance-based approach exhibits a more localized effect, focusing primarily on the designated target points. Nevertheless, even the distance-based approach provides noticeable enhancement compared to the no RIS scenario in the case of -100 dB minimum power threshold.

Furthermore, increasing the RIS size for the distance-based approach improves the power of the low-power cells. However, for moderate power level cells, the performance variation between different RIS size cases is negligible. For the gradient-based approach, performance improvements persist across moderate power level cells as well, since a larger RIS size allows for broader coverage of surrounding areas. This difference arises because the gradient-based
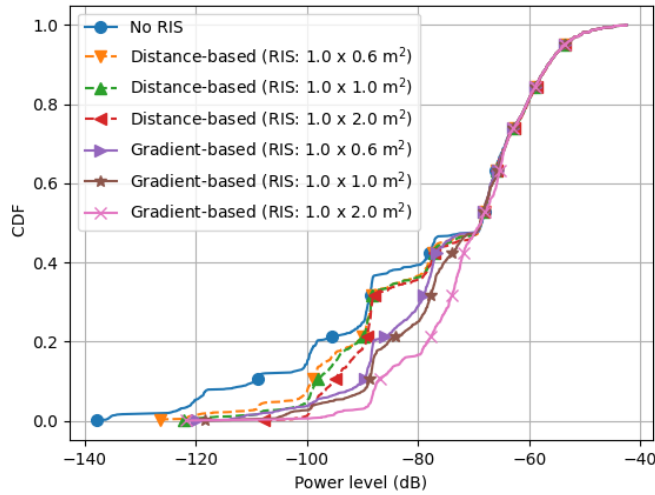
FIGURE 10. Cumulative distribution functions (CDFs) of power levels for different phase profile approaches and RIS sizes, with a minimum power threshold of -100 **dB**

a) Combined coverage map

b) RIS coverage gain

c) Updated binary poor coverage map

FIGURE 11. Combined coverage analysis for a RIS of size 1×2 **m²** using the gradient-based approach, with a minimum power threshold of -100 **dB**

approach not only optimizes power at the target points but also contributes to enhancing the power levels of neighboring cells, whereas the distance-based approach maintains a more focused beam focusing strategy.

As expected, high-power-level cells remain unaffected by the RIS placement since they are already well covered by the transmitter, and the RIS does not specifically target these areas. This observation further emphasizes that the RIS primarily benefits low-power and moderate-power regions, rather than areas that are already sufficiently illuminated by the direct transmitter signal.

4) COMBINED COVERAGE ANALYSIS WITH RIS

To further evaluate the impact of RIS placement, we analyze the combined coverage maps of the transmitter and the RIS for a specific configuration. Fig.s 11 and 12 illustrate the results for the gradient-based and distance-based approaches, respectively.

Fig. 11 presents the results for the gradient-based approach, where the RIS is configured with a size of 1×2 m² and positioned at its sub-optimal location, as identified in Fig. 8. The RIS serves two target points, marked by red 'x' signs, while its placement is indicated by star symbols. The combined coverage map in Fig. 11-a demonstrates that the RIS successfully enhances the power levels at the target points while also improving signal strength along the beam paths. To better quantify this enhancement, the RIS coverage gain in Fig. 11-b highlights significant power level improvements, particularly at the far edge of the lower hallway and within the internal room where the target points are located. Finally, Fig. 11-c shows the updated binary poor coverage map, demonstrating that nearly all cells achieve sufficient power coverage, with a coverage ratio of 99.58% and an increased average power of low-power cells reaching -76.05 dB compared to a coverage ratio of 81.54% and
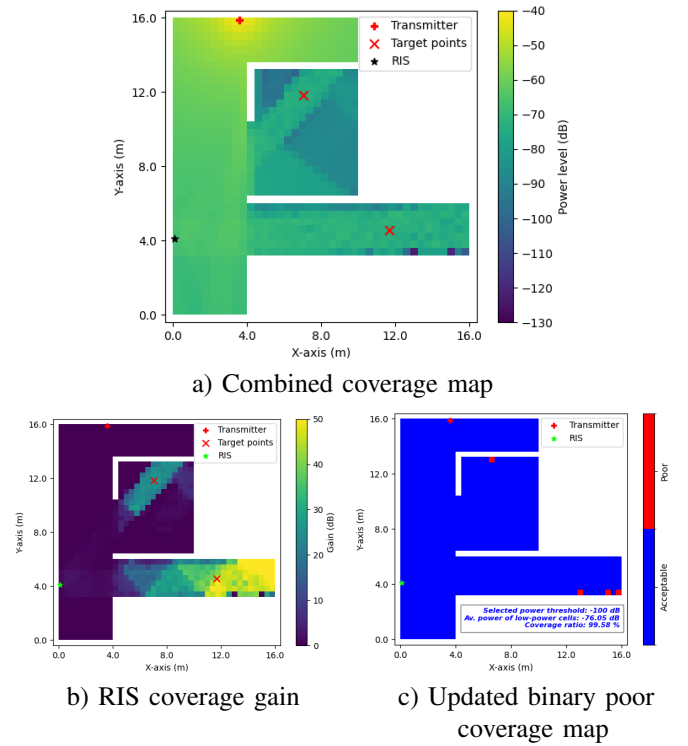
an average power of low-power cells of -112.58 dB in the transmitter-only coverage map.

A similar analysis is conducted for the distance-based approach, as illustrated in Fig. 12. The RIS configuration follows the sub-optimal parameters obtained from the optimization algorithm, where the RIS is positioned at the location indicated by star symbols and assigned three target points. As shown in Fig. 12, the distance-based approach directs energy to narrow regions around the target points. Unlike the gradient-based approach, this method does not significantly enhance power levels outside the focused target point areas. Consequently, some low-power cells, particularly in the large blind spot of the lower hallway, remain uncovered despite the RIS placement. This outcome is specific to the given scenario, where a large blind spot region exists, however, in cases with smaller blind spot areas, the distance-based approach could also yield superior results. Nevertheless, the binary poor coverage map in Fig. 12-c indicates that the average power of low-power cells increases to -89.6 dB, with a gain of nearly 23 dB, while the coverage ratio of the scene reaches 96.31%.

This highlights the trade-offs between the two approaches. While the gradient-based approach provides a more distributed power enhancement, the distance-based approach focuses energy more precisely on the assigned target points. The performance of these methods may also depend on the scenario, as we will explore in the next subsection by
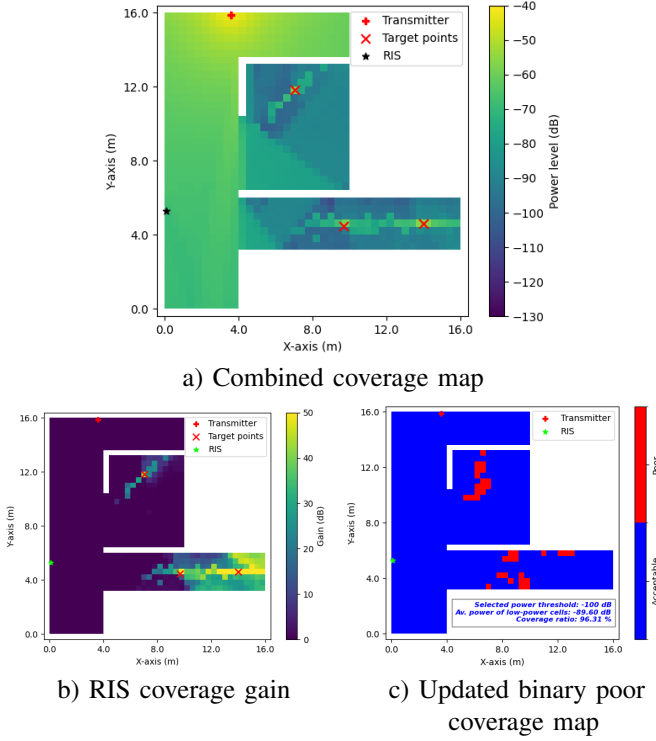
a) Combined coverage map

b) RIS coverage gain

c) Updated binary poor coverage map

FIGURE 12. Combined coverage analysis for a RIS of size 1×2 **m^2 using the distance-based approach, with a minimum power threshold of** -100 **dB**

lowering the minimum power threshold to -110 dB to focus on the weakest signal regions.

F. RESULTS FOR MINIMUM POWER THRESHOLD OF -110 *dB*

In this subsection, we analyze the impact of reducing the minimum power threshold to -110 dB, focusing on the weakest signal regions and their blind spots. This analysis follows a similar methodology to the -100 dB case but reveals different outcomes due to the updated power threshold.

Fig. 13 presents the binary poor coverage maps for different numbers of target configurations when the minimum power threshold is set at -110 dB. The low-power cells in this setting are primarily located at the far edge of the lower hallway, whereas the previously identified low-power cells within the internal room are no longer present. This is because the power levels in that region predominantly fall between -100 dB and -110 dB, making them non-critical under the new threshold. Consequently, the RIS optimization now focuses only on the far edge of the lower hallway with a smaller blind spot region. Considering only the transmitter's contribution, the average power of these newly identified low-power cells is calculated as -121.87 dB, with an initial coverage ratio of 90.40%.

Following the identification of new low-power cells and their corresponding target points, we execute RIS placement and performance evaluations across all feasible locations using the proposed optimization algorithm. Similar to the
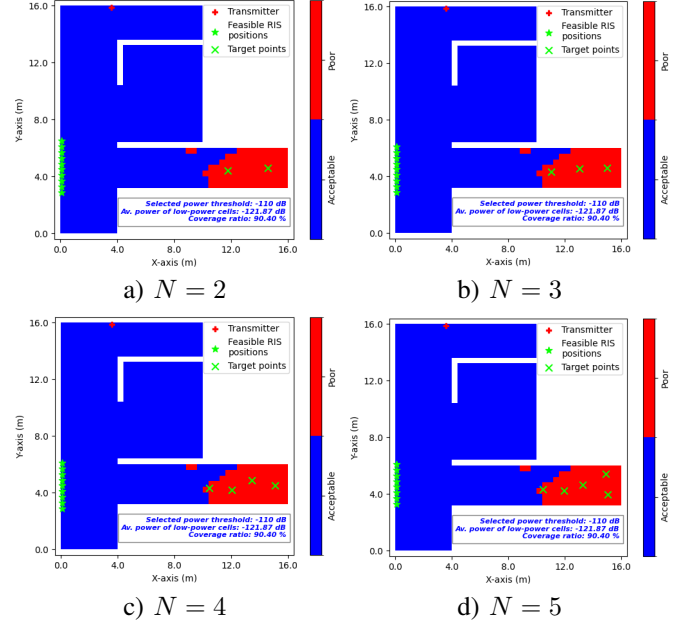

a) $N = 2$

b) $N = 3$

c) $N = 4$

d) $N = 5$

FIGURE 13. Binary poor coverage maps for different number of target configurations for the minimum power threshold of -110 **dB**
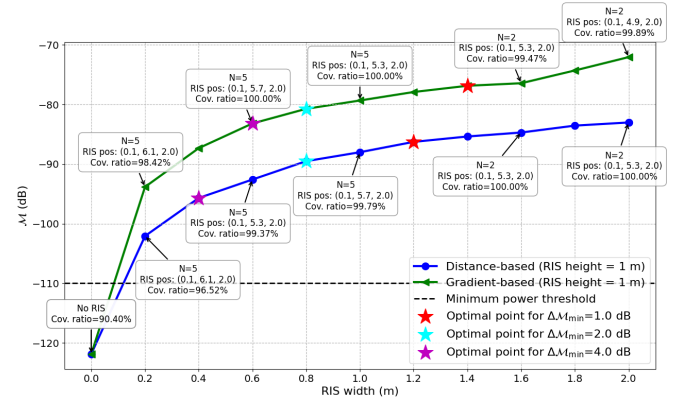

FIGURE 14. Performance metric $\mathcal{M}$ **vs. RIS width plot, showing selected sub-optimal configurations for different performance improvement thresholds** $\triangle \mathcal{M}_{\text{min}}$ **with an RIS height of** 1 **m and a minimum power threshold of** -110 **dB**

previous case, the results of the performance metric $\mathcal{M}$ as a function of RIS width are illustrated in Fig. 14, comparing gradient-based and distance-based approaches. Given the fewer number of low-power cells, all located within the same blind spot, satisfactory coverage improvement is achieved even with a relatively small RIS width for both approaches. While the coverage ratio reaches nearly 100% for most RIS configurations, the gradient-based approach still provides a higher average power level for the low-power cells compared to the distance-based approach.

The cumulative distribution functions (CDFs) of power levels for different phase profile approaches and RIS sizes with a minimum power threshold of -110 dB are presented in Fig. 15. The observed trends are consistent with the previous CDF analysis for the -100 dB case. The major
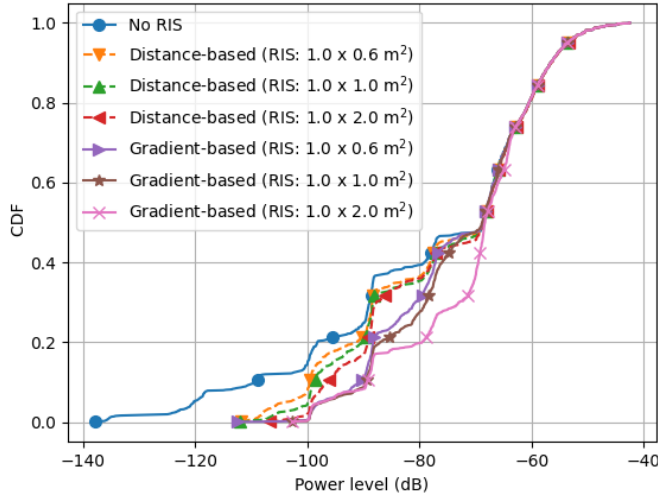
FIGURE 15. Cumulative distribution functions (CDFs) of power levels for different phase profile approaches and RIS sizes, with a minimum power threshold of -110 **dB**

distinction in this scenario is that the lowest-power cells are almost entirely served with the RIS placement such that almost no cells below the level of -110 dB appear. This occurs because the RIS optimization process prioritizes the weakest signal regions by setting a lower power threshold. These results emphasize that if the primary objective is to address severe signal quality issues, selecting a lower minimum power threshold is essential to accurately identify and enhance the most critical low-power regions.

The combined coverage maps for the gradient-based and distance-based approaches with a minimum power threshold of -110 dB are shown in Figs. 16 and 17, respectively. The similar conclusions can be made for the gradient-based approach, it continues to enhance power levels over a broader region. A significant difference is observed for the distance-based approach in Fig. 17, where full coverage is achieved by focusing on two target points. Compared to the previous case with a -100 dB threshold, this setting results in fewer low-power cells concentrated in a smaller blind spot. Consequently, the distance-based approach is particularly effective in scenarios where blind spots are small and all low-power cells are close to the selected target points of the RIS. Ultimately, the updated binary poor coverage maps confirm that nearly full coverage is achieved across the scene.

VI. CONCLUSION

This paper presents a ray-tracing based joint optimization framework for RIS deployment in indoor wireless environments, addressing the critical problem of optimizing RIS position, size, and beam-steering target points. Unlike prior studies that assume fixed RIS positions or arbitrary sizes, our approach systematically determines all key RIS parameters in a unified framework while considering both LoS and non-LoS paths. By leveraging a clustering-based method to identify low-power regions and incorporating a performance-
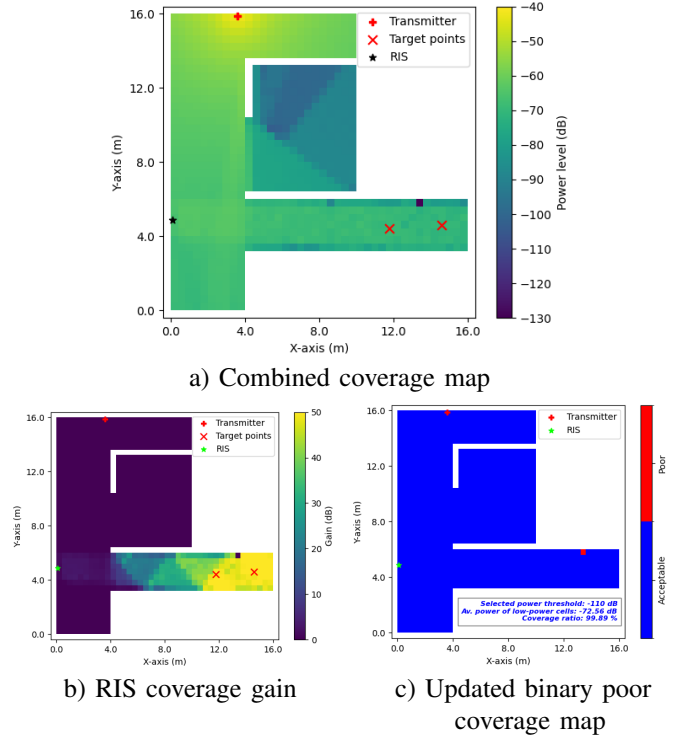

a) Combined coverage map

b) RIS coverage gain

c) Updated binary poor coverage map

FIGURE 16. Combined coverage analysis for a RIS of size 1×2 **m^2 using the gradient-based approach, with a minimum power threshold of** -110 **dB**

a) Combined coverage map

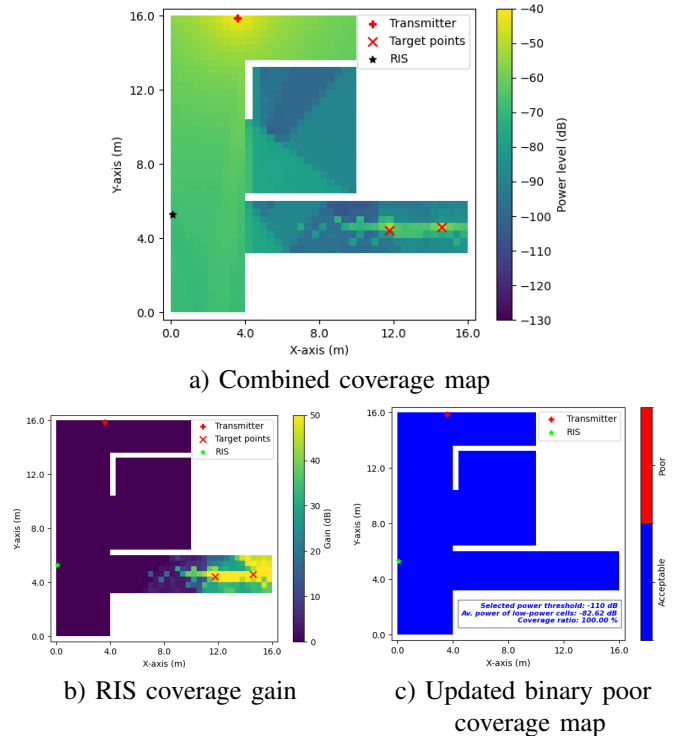b) RIS coverage gain

c) Updated binary poor coverage map

FIGURE 17. Combined coverage analysis for a RIS of size 1×2 **m^2 using the distance-based approach, with a minimum power threshold of** -110 **dB**

cost trade-off strategy for RIS size selection, the proposed algorithm enhances indoor coverage while maintaining computational efficiency. Simulation results demonstrate that our framework significantly improves coverage in blind spots compared to conventional fixed-position RIS deployments. Future work may extend this study to multi-RIS deployments, where multiple RISs collaboratively optimize coverage over a larger indoor area.

REFERENCES

[1] Q. Wu and R. Zhang, "Towards Smart and Reconfigurable Environment: Intelligent Reflecting Surface Aided Wireless Network," *IEEE Communications Magazine*, vol. 58, no. 1, pp. 106-112, January 2020.

[2] E. Basar, M. Di Renzo, J. De Rosny, M. Debbah, M. -S. Alouini and R. Zhang, "Wireless Communications Through Reconfigurable Intelligent Surfaces," IEEE Access, vol. 7, pp. 116753-116773, 2019.

[3] M. Di Renzo et al., "Smart Radio Environments Empowered by Reconfigurable Intelligent Surfaces: How It Works, State of Research, and The Road Ahead," *IEEE Journal on Selected Areas in Communications*, vol. 38, no. 11, pp. 2450-2525, Nov. 2020

[4] M. A. ElMossallamy, H. Zhang, L. Song, K. G. Seddik, Z. Han and G. Y. Li, "Reconfigurable Intelligent Surfaces for Wireless Communications: Principles, Challenges, and Opportunities," IEEE Transactions on Cognitive Communications and Networking, vol. 6, no. 3, pp. 990-1002, Sept. 2020.

[5] Q. Wu, S. Zhang, B. Zheng, C. You and R. Zhang, "Intelligent Reflecting Surface-Aided Wireless Communications: A Tutorial," *IEEE Transactions on Communications*, vol. 69, no. 5, pp. 3313-3351, May 2021.

[6] Ö. Özdogan, E. Björnson and E. G. Larsson, "Intelligent Reflecting Surfaces: Physics, Propagation, and Pathloss Modeling," *IEEE Wireless Commun. Letters*, vol. 9, no. 5, pp. 581-585, May 2020.

[7] S. W. Ellingson, "Path Loss in Reconfigurable Intelligent Surface-Enabled Channels," *2021 IEEE 32nd Annual International Symposium on Personal, Indoor and Mobile Radio Communications (PIMRC)*, Helsinki, Finland, pp. 829-835, 2021.

[8] W. Tang *et al.*, "Wireless Communications With Reconfigurable Intelligent Surface: Path Loss Modeling and Experimental Measurement," *IEEE Trans. on Wireless Commun.*, vol. 20, no. 1, pp. 421-439, Jan. 2021.

[9] C. Pan *et al.*, "Reconfigurable Intelligent Surfaces for 6G Systems: Principles, Applications, and Research Directions," *IEEE Commun. Mag.*, vol. 59, no. 6, pp. 14-20, June 2021.

[10] E. M. Vitucci, M. Albani, S. Kodra, M. Barbiroli and V. Degli-Esposti, "An Efficient Ray-Based Modeling Approach for Scattering From Reconfigurable Intelligent Surfaces," *IEEE Trans. on Antennas and Prop.*, vol. 72, no. 3, pp. 2673-2685, March 2024.

[11] C. You, B. Zheng, W. Mei and R. Zhang, "How to Deploy Intelligent Reflecting Surfaces in Wireless Network: BS-Side, User-Side, or Both Sides?," in Journal of Communications and Information Networks, vol. 7, no. 1, pp. 1-10, March 2022.

[12] C. You and R. Zhang, "Wireless Communication Aided by Intelligent Reflecting Surface: Active or Passive?," in IEEE Wireless Communications Letters, vol. 10, no. 12, pp. 2659-2663, Dec. 2021.

[13] Q. Wu and R. Zhang, "Intelligent Reflecting Surface Enhanced Wireless Network via Joint Active and Passive Beamforming," *IEEE Trans. on Wireless Commun.*, vol. 18, no. 11, pp. 5394-5409, Nov. 2019.

[14] Q. Wu and R. Zhang, "Beamforming Optimization for Intelligent Reflecting Surface with Discrete Phase Shifts," *ICASSP 2019 - 2019 IEEE International Conf. on Acoustics, Speech and Signal Processing (ICASSP)*, Brighton, UK, pp. 7830-7833, 2019.

[15] H. Wang, C. Liu, Z. Shi, Y. Fu and R. Song, "On Power Minimization for IRS-Aided Downlink NOMA Systems," *IEEE Wireless Commun. Letters*, vol. 9, no. 11, pp. 1808-1811, Nov. 2020.

[16] S. Abeywickrama, R. Zhang and C. Yuen, "Intelligent Reflecting Surface: Practical Phase Shift Model and Beamforming Optimization," *ICC 2020 - 2020 IEEE International Conference on Communications (ICC)*, Dublin, Ireland, pp. 1-6, 2020.

[17] H. Yang et al., "Intelligent Reflecting Surface Assisted Anti-Jamming Communications: A Fast Reinforcement Learning Approach," *IEEE Trans. on Wireless Commun.*, vol. 20, no. 3, pp. 1963-1974, March 2021.

[18] K. Feng, Q. Wang, X. Li and C. -K. Wen, "Deep Reinforcement Learning Based Intelligent Reflecting Surface Optimization for MISO Communication Systems," *IEEE Wireless Commun. Letters*, vol. 9, no. 5, pp. 745-749, May 2020.

[19] M. Cui, G. Zhang and R. Zhang, "Secure Wireless Communication via Intelligent Reflecting Surface," *IEEE Wireless Commun. Letters*, vol. 8, no. 5, pp. 1410-1414, Oct. 2019.

[20] A. Zappone, M. Di Renzo, X. Xi and M. Debbah, "On the Optimal Number of Reflecting Elements for Reconfigurable Intelligent Surfaces," *IEEE Wireless Commun. Letters*, vol. 10, no. 3, pp. 464-468, March 2021.

[21] H. Zhang, B. Di, Z. Han, H. V. Poor and L. Song, "Reconfigurable Intelligent Surface Assisted Multi-User Communications: How Many Reflective Elements Do We Need?," *IEEE Wireless Commun. Letters*, vol. 10, no. 5, pp. 1098-1102, May 2021.

[22] M. D. Nguyen, L. B. Le and A. Girard, "UAV Placement and Resource Allocation for Intelligent Reflecting Surface Assisted UAV-Based Wireless Networks," IEEE Communications Letters, vol. 26, no. 5, pp. 1106-1110, May 2022.

[23] X. Gu, G. Zhang, W. Duan, M. Wen, J. Choi and P. -H. Ho, "ARIS-Empowered Wireless Communications: Joint Beamforming Design and Deployment Optimization," IEEE Wireless Communications Letters, vol. 12, no. 12, pp. 2003-2007, Dec. 2023.

[24] H. Nguyen-Kha, H. V. Nguyen, M. T. P. Le and O. -S. Shin, "Joint UAV Placement and IRS Phase Shift Optimization in Downlink Networks," IEEE Access, vol. 10, pp. 111221-111231, 2022.

[25] B. Shang, E. S. Bentley and L. Liu, "UAV Swarm-Enabled Aerial Reconfigurable Intelligent Surface: Modeling, Analysis, and Optimization," IEEE Transactions on Communications, vol. 71, no. 6, pp. 3621-3636, June 2023.

[26] L. Ge, H. Zhang and J. Wang, "Joint Placement and Beamforming Design in Multi-UAV-IRS Assisted Multiuser Communication," 2021 IEEE Global Communications Conference (GLOBECOM), Madrid, Spain, pp. 01-06, 2021.

[27] T. Zhou, K. Xu, X. Xia, W. Xie and J. Xu, "Achievable Rate Optimization for Aerial Intelligent Reflecting Surface-Aided Cell-Free Massive MIMO System," IEEE Access, vol. 9, pp. 3828-3837, 2021.

[28] J. Bai, H. -M. Wang and P. Liu, "Robust IRS-Aided Secrecy Transmission With Location Optimization," *IEEE Transactions on Communications*, vol. 70, no. 9, pp. 6149-6163, Sept. 2022.

[29] H. Guo, Z. Yang, Y. Zou, B. Lyu, Y. Jiang and L. Hanzo, "Joint Reconfigurable Intelligent Surface Location and Passive Beamforming Optimization for Maximizing the Secrecy-Rate," IEEE Transactions on Vehicular Technology, vol. 72, no. 2, pp. 2098-2110, Feb. 2023.

[30] P. S. Aung, Y. M. Park, Y. K. Tun, Z. Han and C. S. Hong, "Energy-Efficient Communication Networks via Multiple Aerial Reconfigurable Intelligent Surfaces: DRL and Optimization Approach," IEEE Transactions on Vehicular Technology, vol. 73, no. 3, pp. 4277-4292, March 2024.

[31] H. Qin, Z. Liu and C. Yang, "Indoor mm-Wave Coverage Enhancement: Reconfigurable Intelligent Surface Deployment Strategy Based on Human Mobility Model," IEEE Communications Letters, vol. 26, no. 10, pp. 2475-2479, Oct. 2022.

[32] J. Feng, B. Zheng, C. You, P. Chen, X. Xiong and F. Chen, "6D Deployment Optimization for Intelligent Reflecting Surface-Aided Wireless Communication," IEEE Wireless Communications Letters, doi: 10.1109/LWC.2024.3524592.

[33] J. Feng et al., "Joint Passive Beamforming and Deployment Design for Dual Distributed-IRS Aided Communication," IEEE Transactions on Vehicular Technology, vol. 72, no. 10, pp. 13758-13763, Oct. 2023.

[34] H. Lu, Y. Zeng, S. Jin and R. Zhang, "Aerial Intelligent Reflecting Surface: Joint Placement and Passive Beamforming Design With 3D Beam Flattening," IEEE Transactions on Wireless Communications, vol. 20, no. 7, pp. 4128-4143, July 2021.

[35] J. Bai, Q. Yan, H. -M. Wang and Y. Liu, "Intelligent Reflecting Surface Aided Green Communication With Deployment Optimization," IEEE Transactions on Communications, vol. 72, no. 8, pp. 5130-5144, Aug. 2024.

[36] F. Naeem, M. Qaraqe and H. Celebi, "Joint Deployment Design and Phase Shift of IRS-Assisted 6G Networks: An Experience-Driven Approach," IEEE Internet of Things Journal, vol. 10, no. 20, pp. 17647-17655, 15 Oct.15, 2023.

[37] N. U. Saqib, S. Hou, S. H. Chae and S. -W. Jeon, "RIS-Aided Wireless Indoor Communication: Sum Rate Maximization via RIS Placement Optimization," ICC 2023 - IEEE International Conference on Communications, Rome, Italy, pp. 511-516, 2023.

[38] N. U. Saqib, S. Hou, S. H. Chae and S. -W. Jeon, "Reconfigurable Intelligent Surface Aided Hybrid Beamforming: Optimal Placement and Beamforming Design," IEEE Transactions on Wireless Communications, vol. 23, no. 9, pp. 12003-12019, Sept. 2024.

[39] S. Zeng, H. Zhang, B. Di, Z. Han and L. Song, "Reconfigurable Intelligent Surface (RIS) Assisted Wireless Coverage Extension: RIS Orientation and Location Optimization," *IEEE Commun. Letters*, vol. 25, no. 1, pp. 269-273, Jan. 2021.

[40] J. Rani, D. Mishra, G. Prasad, A. Hossain, S. De and K. Deka, "Joint Optimization of IRS Location and Passive Beamforming for Enhanced Received Power," IEEE Transactions on Green Communications and Networking, vol. 8, no. 4, pp. 1970-1984, Dec. 2024.

[41] X. Cheng et al., "Joint Optimization for RIS-Assisted Wireless Communications: From Physical and Electromagnetic Perspectives," IEEE Transactions on Communications, vol. 70, no. 1, pp. 606-620, Jan. 2022.

[42] C. Liu et al., "Reconfigurable Intelligent Surface Assisted High-Speed Train Communications: Coverage Performance Analysis and Placement Optimization," IEEE Transactions on Vehicular Technology, vol. 73, no. 3, pp. 3750-3766, March 2024.

[43] J. Zhang and D. M. Blough, "Optimizing Coverage with Intelligent Surfaces for Indoor mmWave Networks," IEEE INFOCOM 2022 - IEEE Conference on Computer Communications, London, United Kingdom, pp. 830-839, 2022.

[44] S. Hou, N. U. Saqib, S. H. Chae, Z. Dou and S. -W. Jeon, "Optimal Placement of Reconfigurable Intelligent Surface for Millimeter-Wave Indoor Communication," 2022 13th International Conference on Information and Communication Technology Convergence (ICTC), Jeju Island, Republic of Korea, pp. 698-700, 2022.

[45] W. Mei and R. Zhang, "Multi-IRS Deployment Optimization for Enhanced Wireless Coverage: A Performance-Cost Trade-off," ICC 2023 - IEEE International Conference on Communications, Rome, Italy, pp. 2056-2061, 2023.

[46] W. Mei and R. Zhang, "Joint Base Station and IRS Deployment for Enhancing Network Coverage: A Graph-Based Modeling and Optimization Approach," IEEE Transactions on Wireless Communications, vol. 22, no. 11, pp. 8200-8213, Nov. 2023.

[47] C. N. Efrem and I. Krikidis, "Joint IRS Location and Size Optimization in Multi-IRS Aided Two-Way Full-Duplex Communication Systems," IEEE Transactions on Wireless Communications, vol. 22, no. 10, pp. 6518-6533, Oct. 2023.

[48] D. Li, "How Many Reflecting Elements Are Needed for Energy- and Spectral-Efficient Intelligent Reflecting Surface-Assisted Communication," IEEE Transactions on Communications, vol. 70, no. 2, pp. 1320-1331, Feb. 2022.

[49] S. Deb and S. C. Ghosh, "An RIS Deployment Strategy to Overcome Static Obstacles in Millimeter Wave D2D Communication," 2021 IEEE 20th International Symposium on Network Computing and Applications (NCA), Boston, MA, USA, pp. 1-8, 2021.

[50] P. -Q. Huang, Y. Zhou, K. Wang and B. -C. Wang, "Placement Optimization for Multi-IRS-Aided Wireless Communications: An Adaptive Differential Evolution Algorithm," *IEEE Wireless Communications Letters*, vol. 11, no. 5, pp. 942-946, May 2022.

[51] A. Khaled, A. S. Alwakeel, A. M. Shaheen, M. M. Fouda and M. I. Ismail, "Placement Optimization and Power Management in a Multiuser Wireless Communication System With Reconfigurable Intelligent Surfaces," IEEE Open Journal of the Communications Society, vol. 5, pp. 4186-4206, 2024.

[52] X. Liu, L. Xue, S. Sun and M. Tao, "Optimization of RIS Placement for Satellite-to-Ground Coverage Enhancement," *2023 IEEE Globecom Workshops (GC Wkshps)*, Kuala Lumpur, Malaysia, pp. 299-304, 2023.

[53] L. Pang, J. Liu, Y. Zhang, X. Liu, Y. Chen and A. Wang, "Deployment Locations and Beamforming Optimization for Multi-RIS in Multi-BS Networks," 2023 IEEE 98th Vehicular Technology Conference (VTC2023-Fall), Hong Kong, Hong Kong, pp. 1-6, 2023.

[54] M. Misbah, Z. Kaleem, W. Khalid, C. Yuen and A. Jamalipour, "Phase and 3-D Placement Optimization for Rate Enhancement in RIS-Assisted UAV Networks," *IEEE Wireless Communications Letters*, vol. 12, no. 7, pp. 1135-1138, July 2023.

[55] H. Lu, H. Zhuang, L. Zhang and Z. Wang, "Gridding Based Reconfigurable Intelligent Surface-aided Wireless Network Optimization," *2024 IEEE 35th International Symposium on Personal, Indoor and Mobile Radio Communications (PIMRC)*, Valencia, Spain, pp. 1-6, 2024.

[56] Q. Chang, G. Nie, H. Tian, G. Li and B. Zhang, "A Sequential-Fairness RIS Deployment for Indoor Multi-User Systems," 2023 IEEE/CIC International Conference on Communications in China (ICCC), Dalian, China, pp. 1-6, 2023.

[57] Z. Li, O. A. Topal, Ö. T. Demir, E. Björnson and C. Cavdar, "mmWave Coverage Extension Using Reconfigurable Intelligent Surfaces in Indoor Dense Spaces," *ICC 2023 - IEEE International Conference on Communications*, Rome, Italy, pp. 5805-5810, 2023.

[58] A. Albanese, G. Encinas-Lago, V. Sciancalepore, X. Costa-Pérez, D. -T. Phan-Huy and S. Ros, "RIS-Aware Indoor Network Planning: The Rennes Railway Station Case," *ICC 2022 - IEEE International Conference on Communications*, Seoul, Korea, Republic of, pp. 2028-2034, 2022.

[59] J. Huang, C. -X. Wang, Y. Sun, J. Huang and F. -C. Zheng, "A Novel Ray Tracing Based 6G RIS Wireless Channel Model and RIS Deployment Studies in Indoor Scenarios," *2022 IEEE 33rd Annual International Symposium on Personal, Indoor and Mobile Radio Communications (PIMRC)*, Kyoto, Japan, pp. 884-889, 2022.

[60] E. Kilcioglu and C. Oestges, "Ray-Tracing Based Algorithms for Indoor RIS Optimization and Coverage Enhancement," *to appear in 2025 19th European Conference on Antennas and Propagation (EuCAP)*, 2025, pp. 1-5.

[61] J. Hoydis, S. Cammerer, Fayçal A. A., A. Vem, N. Binder, G. Marcus, and A. Keller, "Sionna: An Open-Source Library for Next-Generation Physical Layer Research", *arXiv*, March 2022, https://arxiv.org/abs/2203.11854.

[62] ITU-R, "Effects of building materials and structures on radiowave propagation above about 100 MHz", *Recommendation ITU-R P.2040-2*.

EMRE KILCIOGLU received his B.Sc. and M.Sc. degrees in Electrical and Electronics Engineering from Middle East Technical University, Ankara, Turkey, in 2016 and 2019, respectively. He completed his Ph.D. in 2024 at the Institute of Information and Communication Technologies, Electronics and Applied Mathematics (ICTEAM), Université catholique de Louvain (UCLouvain), Louvain-la-Neuve, Belgium, where he is currently a postdoctoral researcher. From July 2016 to January 2020, he worked as a system design engineer at Aselsan Inc., Ankara, Turkey. His research interests include massive MIMO, cooperative communication, deep learning applications in wireless communications, and ray-tracing-based optimization of reconfigurable intelligent surfaces (RISs).

CLAUDE OESTGES ...